Mechanically stable monolithic porous boron nitride with high volumetric adsorption capacity

Tian Tian, Jingwei Hou, Humera Ansari, Ying Xiong, Anouk L'Hermitte, David Danaci, Ronny Pini, and Camille Petit*

Dr. T. Tian, Dr. Y. Xiong, A. L'Hermitte, Dr. D. Danaci, Dr. C. Petit
Barrer Centre, Department of Chemical Engineering
Imperial College London, South Kensington Campus
London SW7 2AZ, UK
E-mail: camille.petit@imperial.ac.uk

Dr. J. Hou
School of Chemical Engineering
University of Queensland
QLD 4072, Australia

H. Ansari, Dr. R. Pini
Department of Chemical Engineering
Imperial College London, South Kensington Campus
London SW7 2AZ, UK

A. L'Hermitte
Department of Materials
Imperial College London, South Kensington Campus
London SW7 2AZ, UK

Keywords: porous boron nitride, monolith, density, mechanical strength, gas adsorption, formation mechanism

The development of adsorbents into structured and robust forms remains a challenge for emerging porous materials. In the context of porous boron nitride (BN), studies point to a tradeoff between mechanical stability, porosity, density, and adsorption kinetics. Approaches towards shaping and densification of porous BN have been mostly empirical since a detailed understanding of its formation mechanism, and how it impacts mechanical strength and porosity, is lacking. Here, we demonstrate a synthesis method that can directly produce a mechanically robust monolithic porous BN ($_{mp}$BN) from an easily scalable polymeric precursor, which results in the highest volumetric surface area among porous BN samples to date. $_{mp}$BN exhibits a high bulk density, 50% higher than BN powders and over ten times higher than the structured BN aerogels, while maintaining fast sorption kinetics. $_{mp}$BN presents good mechanical strength,

with hardness of 66.4 ± 4.5 MPa, *i.e.* one to two orders of magnitude higher than structured aerogels. We propose a $_{mp}$BN formation mechanism which reveals that the crosslinked intermediates are responsible for the high mechanical strength of the final material. Our approach produces a form of BN that addresses the limitations of other adsorbents, and facilitate their application in gas separation and storage technologies.

1. Introduction

Owing to their high surface area, large porosity and rich surface functionalities, porous materials (*e.g.* zeolites, activated carbon, and metal-organic frameworks) can be used in a range of applications from catalysis to gas separation, and storage.[1–3] Processing these materials from powders to robust densified structures (*e.g.* pellets, beads, and monoliths) represents a necessary step towards their industrial deployment. Indeed, powders suffer from limited mass transfer and poor mechanical strength and they are difficult to handle at scale.[4,5] The large amount of interparticle space in powders also causes low bulk density and low volumetric adsorption/storage capacity,[6,7] which in turn, leads to an increased footprint.[8,9]

Shaping and densifying powders into mechanically robust structures can be done as follows: (i) mechanical compaction, (ii) application of binders, or (iii) growth on monolithic supports.[7] These approaches usually result in decreased performance due to pore collapse from high-pressure, pore blockage from binders, or 'dead' volume from the support. Recently, Tian *et al.* developed a methodology towards the densification of metal organic frameworks via a sol-gel method without using high-pressure compaction or binders, providing scope for the development of monolithic porous materials.[9] However, the advances of producing other robust porous materials is still lacking, particularly for ceramics.[10]

Amorphous boron nitride (BN) represents a relatively new addition to the porous materials family,[11–16] with recent studies demonstrating its use in molecular separation,[13,17–22] catalysis,[23] and drug delivery.[24] Like other porous materials, identifying a way to shape and

2

densify BN without compromising the porosity is needed. We note increasing focus towards producing structured BN in the recent literature. For example, BN aerogel, the most common form of structured BN, has been synthesized using various methods such as direct chemical reaction,[25,26] carbonaceous template assisted method,[27–29] or molecular substitution.[30] Yet, all structured BN aerogels exhibit low density and mechanical strength, preventing their upscaling for practical adsorption applications. Sintering, another important method to synthesize structured BN, usually leads to a low surface area, albeit with high mechanical strength.[31] Overall, these studies lead to two main observations: (i) a tradeoff persists between mechanical stability, porosity, density and adsorption kinetics; (ii) approaches towards shaping and densification of porous BN have been mostly empirical since a detailed understanding of porous BN formation mechanism and how it impacts mechanical strength and porosity is lacking. We hypothesize that higher bonding densities within BN will allow good resistance to deformation and loading. Hence, monitoring the formation mechanism of porous BN and linking it to mechanical strength will be important towards developing robust densified porous BN structures.

Herein, we present a method to synthesize a *monolithic porous* BN, named $_{mp}$BN, that exhibits high surface area, mechanical strength and enhanced volumetric adsorption capacity compared to powder BN. $_{mp}$BN also shows enhanced hydrolytic stability compared to BN powders, owing to a reduced oxygen content. Our method does not involve any compaction, binding or supporting step but instead relies on the use of a mechanically stable polymer precursor, a melamine-formaldehyde (MF) resin. MF resins have been well-developed at industry scale, making the current synthesis method suitable for upscaling. Through in-depth XPS and FTIR analyzes, we determine the formation mechanism of $_{mp}$BN starting from this polymer and how it influences the resulting mechanical stability.

**2. Results and Discussion**

2.1. Synthesis of monolithic porous BN ($_{mp}$BN)

3

We used a macroporous melamine-formaldehyde (MF) resin as the precursor to produce monolithic porous BN, $_{mp}$BN (**Scheme 1**). To synthezise the resin, we employed dicyandiamide (DCD) as a foaming agent,[32] and boric acid as the curing agent. The pore density in the MF resin was controlled by the DCD content and appears to impact the final morphology of the porous BN (**Figure 1**). Indeed, on the one hand, a low DCD content results in a non- or poorly porous MF resin, as indicated by the low 'bubbles' density observed on the microscope images (Figure S1). We attribute this behavior to the fact that gases generated during pyrolysis could not easily 'escape' through the tight resin, thus leading to pressure build-up and eventually structure collapse (Figure 1a, 1b). On the other hand, a high DCD content formed a highly porous resin (Figure S1). We speculate that the low crosslink density (i.e. high porosity) of the resin meant that it was too fragile to withstand the chemical decomposition and gas release during pyrolysis, leading to the formation of powder (Figures 1e). Overall, we have found that a DCD/melamine weight ratio of 0.72 resulted in a precursor with moderate pore density and high mechanical strength. In this case, the pores act as channels for the porogen to escape while the good crosslink density prevents the collapse of the macrostructure upon pyrolysis. As a result, we obtain a monolithic BN sample (Figure 1c, 1d).
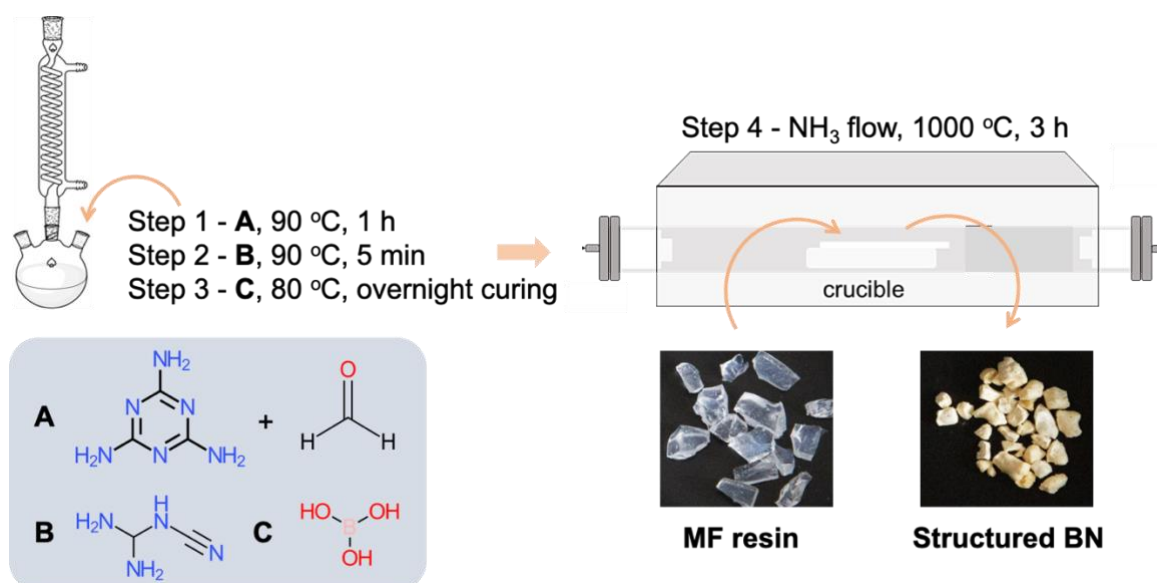
Scheme 1. Schematic representation of monolithic porous BN ($_{mp}$BN) synthesis via the formation of a melamine-formaldehyde resin (MF resin). A = Melamine + Formaldehyde; B = Dicyandiamide, C = Boric acid.
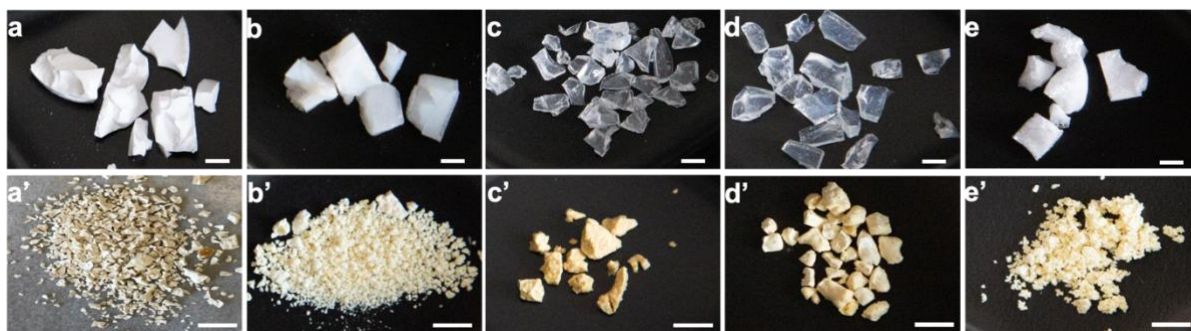
Figure 1. Optical images of the melamine-formaldehyde (MF) resin with different amounts of foaming agent, DCD (a-e), and the derived porous BN samples (a'-e'). DCD/melamine weight ratio of (a) and (a') 0; (b) and (b') 0.24; (c) and (c') 0.48; (d) and (d') 0.72; (e) and (e') 0.96. Scale bar = 1 cm.

Based on the observations above, we then focused our attention on the BN samples obtained using a 0.72 DCD/melamine weight ratio (Figures 1d and S2). We explored the effects of reaction atmosphere, reaction temperature and duration on the pyrolysis product to identify the optimal pyrolysis conditions. Looking first at the reaction atmosphere, we note significant differences between the products obtained under either NH_3 or N_2, starting from the color: yellowish *vs* black, respectively. As shown in Figure S3, the sample obtained under NH_3 exhibits a higher BET specific surface area than that obtained under N_2 (1513 m^2 g^{-1} *vs* 216 m^2 g^{-1}). These differences result from the amount of active N-containing gases (*e.g.* NH_3) during the synthesis. Under N_2, the reactive N source comes principally from the resin and is insufficient for complete reaction with boric acid. Therefore, carbonization is predominant resulting in a black sample with a low surface area. In contrast, the synthesis under NH_3 provides an excess of reactive N over a wide range of temperature, which is known to enhance the surface area of porous BN.[20] Consequently, NH_3 was selected as the reaction atmosphere for further tests.

Next, we investigated the effects of the reaction temperature and the duration of the isothermal step. Keeping the duration at 3 h, the BET specific surface area increased from 1349 m^2 g^{-1} at 800 °C to 1513 m^2 g^{-1} at 1000 °C (**Figure 2**a). Further increasing the reaction temperature to 1200 °C resulted in a decreased BET area (1397 m^2 g^{-1}), possibly due to a partial

crystallization of BN.[13,30] Furthermore, extending the duration of the isothermal step up to 3 h at 1000 °C enhanced the porosity (Figure 2b). Beyond 3 h, the surface area reached a plateau, pointing towards a completion of the reactions leading to the gases release and porosity formation. To summarize, pyrolizing the MF resin in NH_3 atmosphere at 1000 °C for 3 h appeared the most effective method in obtaining $_{mp}BN$ and was used in the current work.
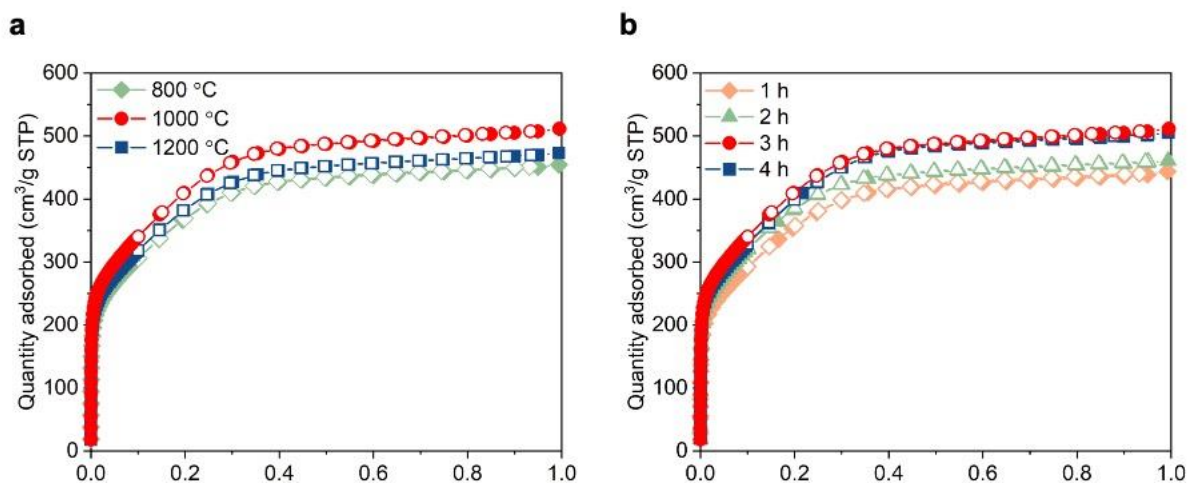

Figure 2. Analysis of the pyrolysis conditions on the porosity of BN. N_2 sorption isotherms of monolithic porous $_{mp}BN$ at 77 K. a) pyrolyzed for 3 h at different temperatures; b) pyrolyzed at 1000 °C for increasing durations.

2.2. Characterization of monolithic porous BN ($_{mp}BN$)

We now analyze in more detail the features of $_{mp}BN$ obtained using the optimal conditions determined above. **Figure 3**a shows the XRD pattern of the sample. The two broad peaks corresponding to (002) and (100) planes together with the absence of other reflections point to the presence of turbostratic/amorphous BN.[30] The two main characteristic IR bands of BN at ~1360 cm⁻¹ (in-plane BN stretching) and ~810 cm⁻¹ (out-of-plane B-N-B bending) are detected (Figure 3b), confirming the chemical composition of $_{mp}BN$.[20] We attribute the additional small band at ~1100 cm⁻¹ to B-O bending mode.[23] The presence of oxygen is further confirmed by XPS analyzes, with a quantity of 3 at% (Figure 3d). The lower oxygen content of $_{mp}BN$ compared to powder BN (3 at% *vs* 9 at%) leads to a significant improvement of hydrolytic stability, an important feature for industrial application, as shown in Figures S4 and S5.[33] SEM

6

image of mpBN (Figure 3c) reveals a continuous solid phase with slender cracks. The compact solid phase presents a relatively flat surface similar to other highly dense monolithic porous materials.[8,9] The morphology is different from that of powders or aerogels, which contain a large amount of interparticle space.[20,29] The slender cracks with macropores are distributed within the continuous flat surface and may result from the pores in the resin precursor. The pores propagated and enlarged under the stress generated during the synthesis, forming these gully-like cracks.
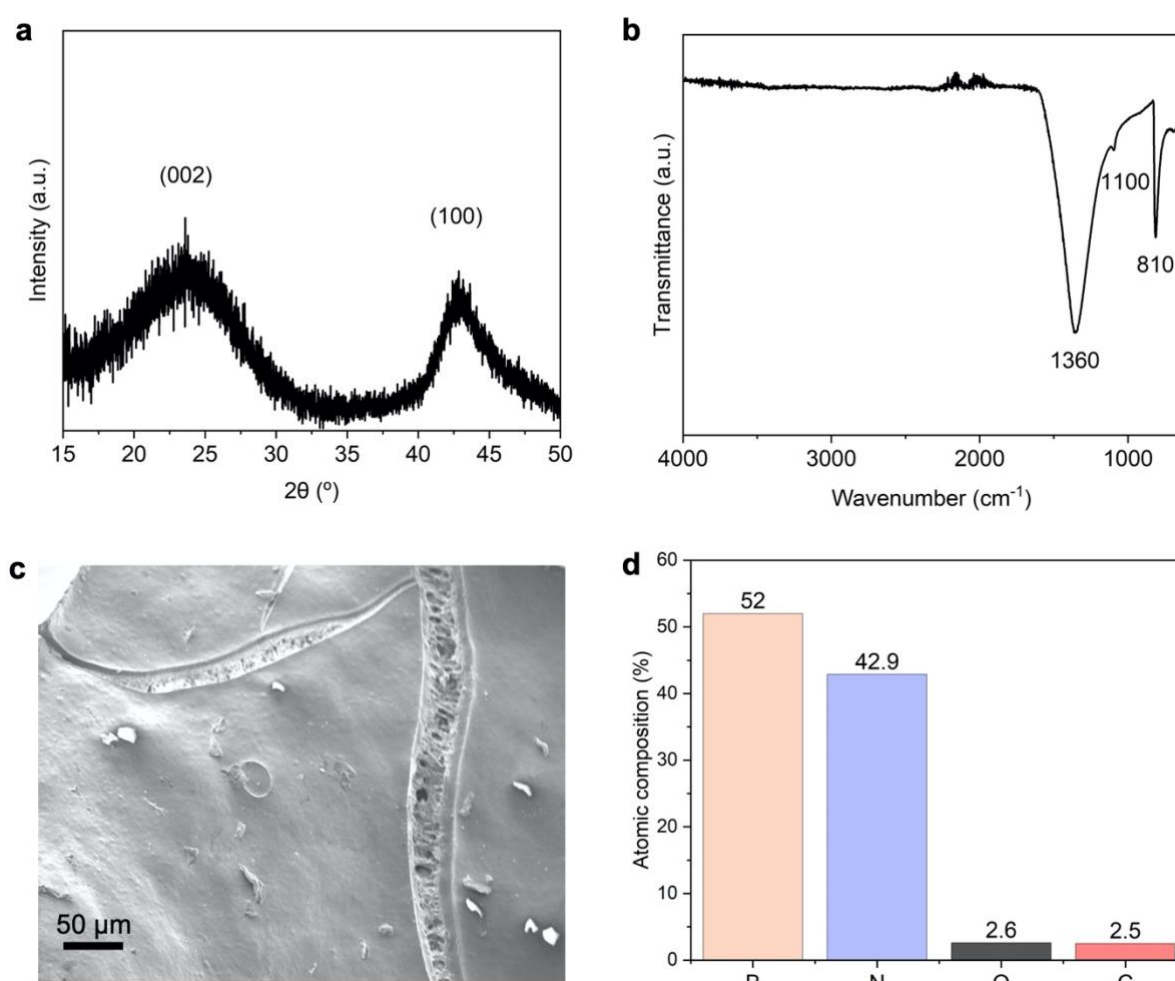
Figure 3. Structure, morphology and surface composition of monolithic porous BN, mpBN. (a) XRD patterns; (b) FTIR spectrum; (c) SEM image; (d) XPS relative atomic percentages.

2.3. Textural and gas adsorption properties of monolithic porous BN (mpBN) vs powder BN

We evaluated the porosity of $_{mp}$BN using the N_2 adsorption isotherms at 77 K and compared it with a highly porous BN powder recently reported by our group (**Table 1**, Figure S6).[20,23] $_{mp}$BN possesses a similar specific surface area to powder BN. However, different to powder BN which exhibits type IV isotherms, $_{mp}$BN exhibits a type I(b) isotherm, typical for materials with both micropores and narrow mesopores.[34] The pore size distribution in Figure S7 shows that the majority of the pores in $_{mp}$BN are < 2.5 nm. Furthermore, N_2 sorption in $_{mp}$BN plateaus for $P/P_0 > 0.5$. On the contrary, N_2 adsorption in powder BN increases towards high P/P_0 values due to N_2 condensation. This is due to the compact nature of $_{mp}$BN, which results in minimal interparticle porosity.

To quantify the compact nature of $_{mp}$BN, we measured its bulk density using mercury porosimetry, a well-established technique that has been used to measure the bulk density of other porous materials.[35] Mercury is a non-wetting liquid that does not intrude small pores at ambient pressure, which facilitates the measurement of bulk volume and thus the density (Section S3.2). Table 1 shows the bulk density of $_{mp}$BN was 0.31 g cm^{-3}, nearly 50 % higher than that of the bulk powder, which leads to a significantly higher volumetric BET area, achieving 473 m^2 cm^{-3} (vs 315 m^2 cm^{-3} for powder BN). We note that structured BN aerogels usually exhibit bulk densities of 0.01-0.02 g cm^{-3},[25,26,36–40] more than one order of magnitude lower than that of $_{mp}$BN, ultimately leading to a low volumetric BET area (i.e. 0.1 – 14 cm^2 cm^{-3}). On the other hand, sintered structured BN typically shows high density but a low BET area (< 450 m^2 g^{-1}),[31] which results in a moderate volumetric BET area similar to the powder BN. $_{mp}$BN therefore exhibits the highest volumetric BET area for a BN sample published to date.

Table 1. Comparison of gravimetric and volumetric properties of monolithic porous BN ($_{mp}$BN) and powder BN. BET area ($S_{BET}(g)$), total pore volume (V_{tot}), micropore volume (V_{micro}) obtained from N_2 sorption isotherms at 77 K and bulk density (ρ) and volumetric BET area (S_{BET} (vol)) derived from mercury porosimetry.

	S_{BET} (mass) [m^2 g^{-1}]	V_{tot} [cm^3 g^{-1}]	V_{micro} [cm^3 g^{-}]	ρ [g cm^{-3}]	S_{BET} (vol) [m^2 cm^{-3}]
Monolithic $_{mp}$BN	1523	0.79	0.56	0.31	473

| Powder BN | 1500 | 1.14 | 0.56 | 0.21 | 315 |

Volumetric methane storage capacity can be attractive for on board applications, where space for fuel is always a constraint. In these cases, the volumetric methane uptake is to be considered. Considering the volumetric properties of $_{mp}$BN, we performed CH_4 adsorption isotherms at 298 K up to 70 bar. **Figure 4**a shows that the absolute gravimetric uptake of $_{mp}$BN is comparable to that of powder BN, owing to the similar surface area and micropore volume. Remarkably, $_{mp}$BN shows a significant enhancement when considering the absolute volumetric adsorption capacity (59 *vs* 42 (STP) cm^3 cm^{-3} at 70 bar) as a result of the higher bulk density of $_{mp}$BN (Figure 4b).

A higher material density often compromises adsorption kinetics due to the mass transfer limitation. To explore the adsorption kinetics of $_{mp}$BN, we measured the adsorption equilibration time of N_2 adsorption at an extremely low pressure (2.2×10^{-6} bar) at 77 K and compared the results to those obtained for the powder sample (Figure S9). At very low pressures, differences in kinetics between the two materials are likely to be the most visible, hence the selection of 2.2×10^{-6} bar for the measurement. Both samples show very fast adsorption kinetics, reaching equilibrium within 60s. The small difference was mainly attributed to the lower macroporosity in $_{mp}$BN, which results in a slightly lower diffusivity.
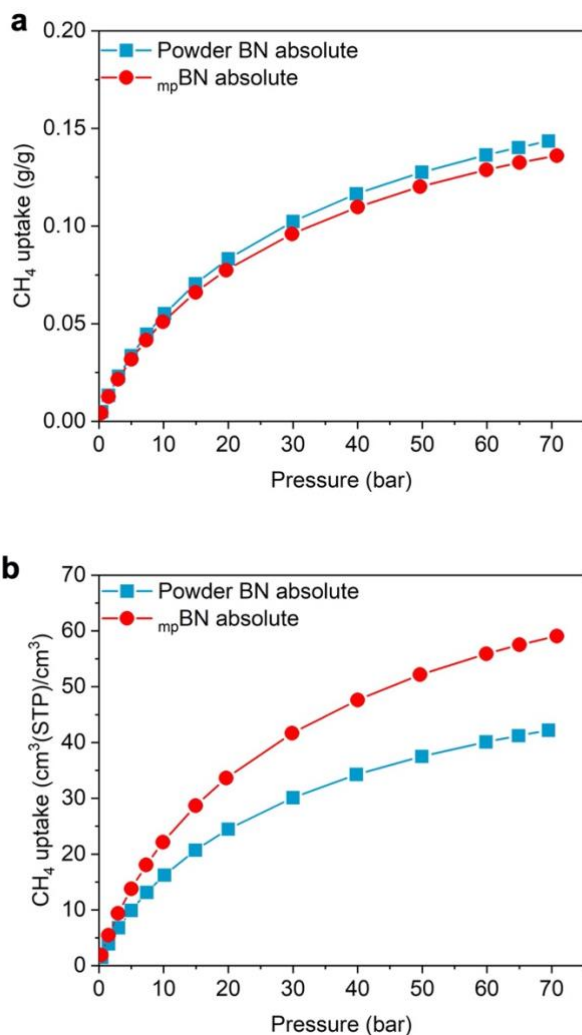
Figure 4. Comparison of absolute methane uptake at 298 K between powder BN (blue squares) and $_{mp}$BN (red circles).

2.4. Mechanical stability of monolithic porous BN ($_{mp}$BN)

Mechanical stability of adsorbents is an important property in practical applications as materials are always exposed to mechanical stress such as operational vibration and compression, i.e. weight of the packed adsorbent. As a preliminary and quick visual test of the mechanical robustness of $_{mp}$BN, we first loaded a calibration weight onto the sample (Figure S10). Ca. 0.005 g of $_{mp}$BN maintained its integral bulk structure under a 200 g calibration weight, pointing to an apparent robustness. We then evaluated quantitatively the hardness of the sample using microindentation. Our results show the hardness of $_{mp}$BN is 66.4 ± 4.5 MPa, which is comparable to dense binder-free graphene oxide pellets[41] and macroporous nickel foam.[42]

Remarkably, the hardness is 1-2 orders of magnitude higher than that reported for BN aerogels,[43,44] suggesting a much higher resistance to plastic deformation, mainly attributed to the higher density.

2.5. Formation mechanism of monolithic porous BN ($_{mp}$BN)

Finally, we aimed to understand the formation mechanism of $_{mp}$BN and its impact on the mechanical stability of the material by analyzing the structural evolution from MF resin to $_{mp}$BN. To do so, we collected samples obtained from the pyrolysis of MF resin under NH_3 at different temperatures: 200, 300, 400, 600, 800 and 1000 °C. We then analyzed the structural and chemical properties of these intermediates. **Figure 5** presents the optical images of the intermediates and highlights significant changes in aspect as the sample subsequently turned brown (300 °C), black (400 and 600 °C), brown (800 °C) and yellow (1000 °C).
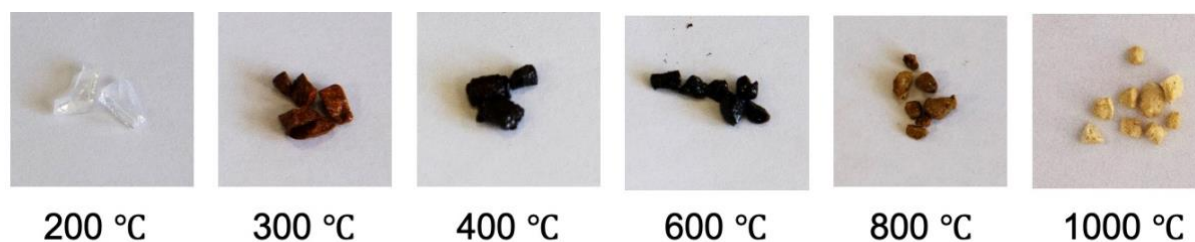
Figure 5. Optical images of melamine-formaldehyde resin (MF resin) heated at increasing temperatures under NH_3 atmosphere.

We used XPS to identify the chemical structure of the intermediates. The core level spectra of B1s, N1s and O1s are presented in **Figure 6**a-c. The intermediate collected at 200 °C shows the typical melamine resin spectrum, namely two peaks located at 339.4 eV (pyrrodic N) and 398.2 eV (pyridinic N), respectively in N1s spectra and one peak at 287.6 eV assigned to triazine ring in C1s spectra.[45,46] The absence of C-O peak suggests the resin is crosslinked *via* methylene bridges rather than ether bridges. Only a single peak at 192.2 eV corresponding to B-O in boron oxide is displayed in B1s spectra, indicating that boron oxide is physically interacted with resin at this temperature but not yet interacting chemically. At 300 °C, we

observe the contribution of B-O-C bonds at 192 eV in B1s spectra.[47,48] The appearance of this new bond is supported by the new C-O peak (286.4 eV) in C1s spectrum, revealing that chemical interactions between boron oxide and the MF resin start at 300 °C. Further increasing the temperature to 400 °C does not alter the B1s spectra. However, the main peak in C1s shifts to a higher binding energy. This observation together with the presence of graphitic N (400.3 eV) in N1s spectrum suggests the evolution from triazine to heptazine likely from the melon-based structure, an intermediate commonly observed in carbon nitride, g-C_3N_4, evolution.[49,50] At 600 °C, we observe the formation of boronoxynitride, an important intermediate in forming porous BN, as evidenced by the new peaks at 191.2 eV (B1s) and 399.6 eV (N1s).[19,44] Our findings show that all the boron atoms chemically interact with the resin skeleton by either via B-O-C or B-O-N bond at 600 °C. BN is subsequently formed at 800 °C, as evidenced by the peaks at 190.6 eV and 398.2 eV from B1s and N1s, respectively. The majority of carbon atoms are removed at this stage as seen in Figure 6d and as suggested by the lighter color of the 800 °C intermediate.[51,52] Further increasing the temperature boosts carbon and oxygen removal and BN conversion through nitridation, resulting in a porous BN with a bright yellow color. The structural evolution above is supported by the analysis from FTIR shown in Figure S11.
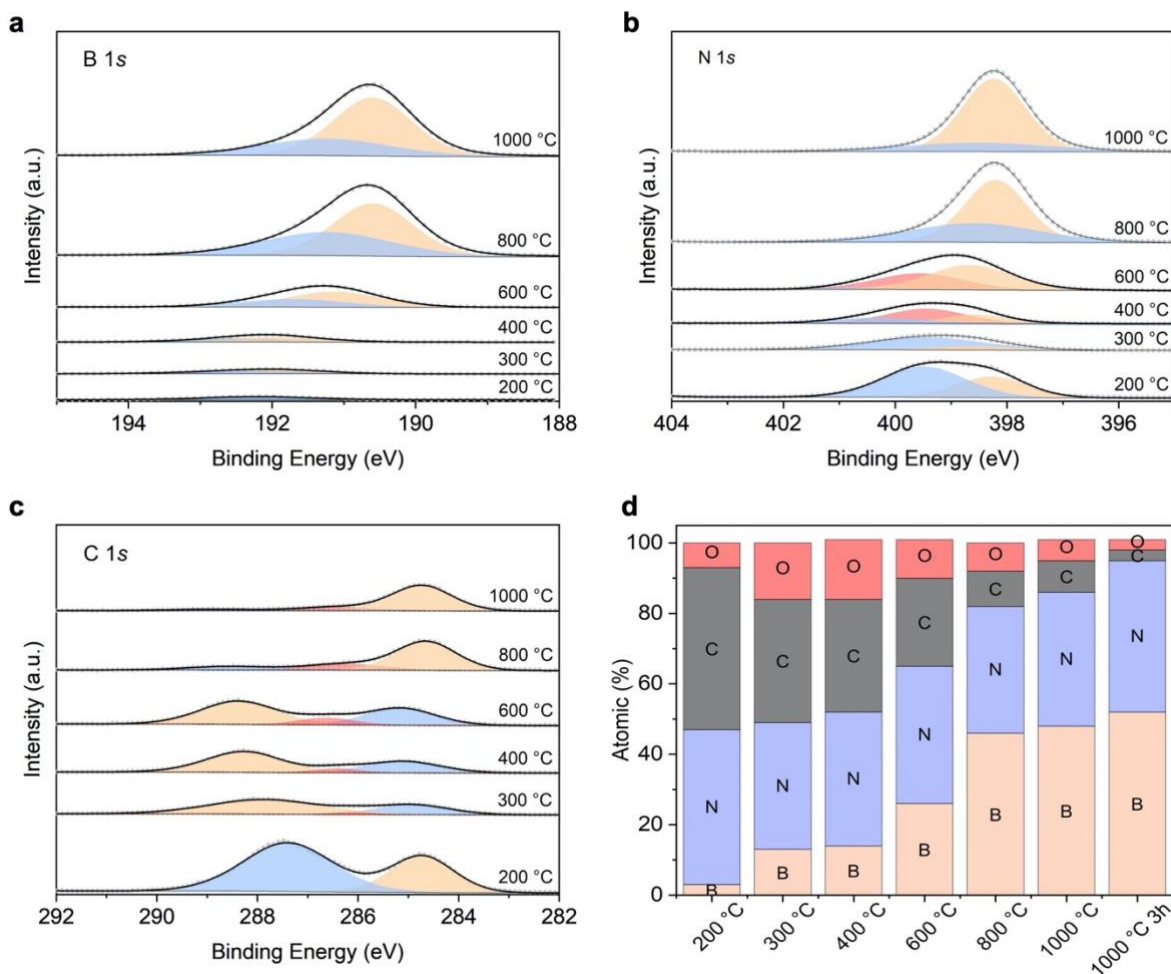
Figure 6. Surface composition of intermediates obtained at different temperatures as determined by high resolution XPS spectra: (a) B 1*s*; (b) N 1*s*; (c) C 1*s*; (d) XPS relative atomic percentage of intermediates.

Based on the analysis above, we propose the structural evolution from MF resin to $_{mp}$BN as shown in **Figure 7**. First, methylene bridged MF resin bonds chemically to boron oxide *via* B-C-O. Then, the formation of a melon-based polymer takes place. Carbon atoms are gradually removed while the remaining compounds retain the crosslinked structure *via* B-O-C and B-O-N bonds. BN is then formed *via* a nitridation process and eventually the monolithic BN with minimum impurities is produced. Throughout $_{mp}$BN formation, a crosslinked structure is maintained. This high bonding density in turns allows mechanical robustness to be preserved in the final product. This structural evolution study paves the way for further engineering of $_{mp}$BN at larger scale.
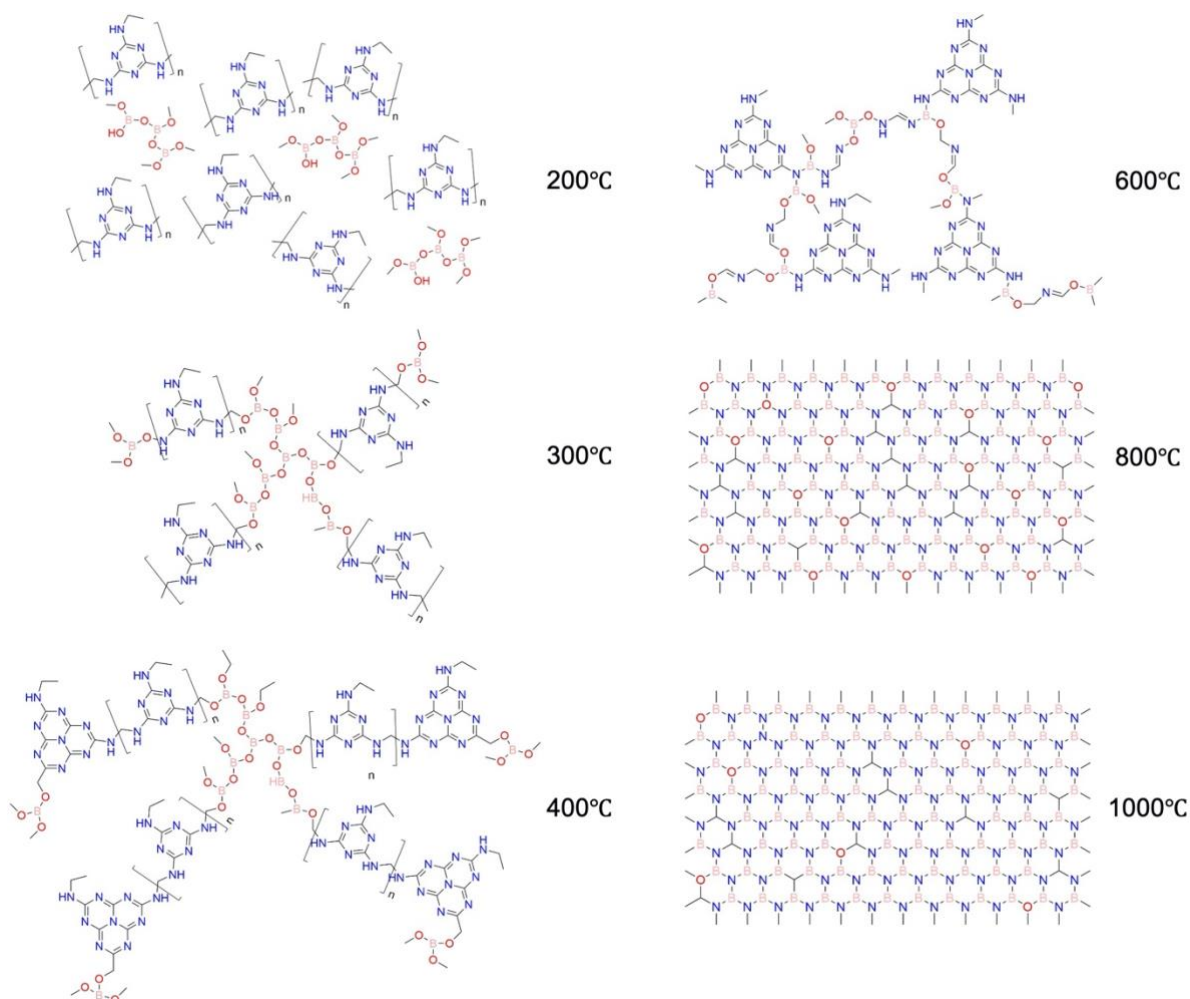
Figure 7. Proposed structural evolution of monolithic porous BN ($_{mp}$BN), using melamine-formaldehyde resin, MF resin, as a precursor and NH_3 as the pyrolysis atmosphere.

3. Conclusion

We have developed a monolithic porous BN ($_{mp}$BN) using a porous melamine-formaldehyde resin (MF resin) as precursor. A suitable range of pore density in the precursor and a NH_3 synthesis atmosphere are necessary to obtain porous $_{mp}$BN. Compared to BN powders, $_{mp}$BN exhibits an improved hydrolytic stability, a 50% higher bulk density and therefore an increased volumetric surface area, the highest among BN materials reported to date. As a result, $_{mp}$BN displays an enhanced volumetric CH_4 adsorption capacity, while sorption kinetics remains fast. $_{mp}$BN shows remarkable mechanical strength (*i.e.* hardness), being one to two orders of magnitude higher than that of aerogels. Studying the $_{mp}$BN formation mechanism, we found that the polymer intermediates derived from the resin crosslink with boron atoms, which impart

the mechanical stability to $_{mp}$BN. The promising properties support the potential of $_{mp}$BN for practical molecular adsorption applications and the formation mechanism study facilitates the industrial scale production of $_{mp}$BN.

4. Experimental Section

Materials: Melamine (99%), and boric acid (≥ 99.5%) were purchased from Sigma-Aldrich; dicyandiamide (99.5%), and formaldehyde solution (37%) were purchased from Fisher. All chemicals were used as received. The gases used in this study, namely NH_3 (99.98%), CH_4 (99.5%), N_2 (99.9995%), and Ar (99.999%) were purchased from BOC.

Synthesis of monolithic porous BN ($_{mp}$BN): A mechanically robust melamine-formaldehyde resin, referred to as MF resin, was used as the precursor to synthezise monolithic porous BN. The overall synthesis procedure is shown in Scheme 1 and described below. To synthezise the MOF resin, formaldehyde (5 mL), NaOH (1 м, 0.15 mL) and melamine (2.08 g) were mixed in a 50 mL round bottom flask and stirred at 90 °C for 1 h. Dicyandiamide (1.5 g) was then added to the transparent solution and stirred for 5 min. Boric acid (1 g) was added to the transparent solution and vigorously stirred for 2 min, followed by a curing step at 80 °C overnight. The collected transparent solid was further dried at 120 °C under vacuum overnight and is referred to as MF resin. The MF resin 'slab' broke into small pieces after vacuum treatment. The MF resin was placed in an alumina boat crucible and transferred to a tubular furnace. The resin was first degassed at room temperature under Ar flow (250 mL min^{-1}). Upon completion of the degassing, the sample was heated to 1000 °C (10 °C min^{-1}) under pure NH_3 gas flow (100 mL min^{-1}) and held isothermally for 3 h, unless otherwise specified. The furnace was cooled naturally under NH_3 to 600 °C and then to room temperature under Ar. Light yellow monoliths were collected after the synthesis and further dried at 120 °C under vacuum overnight.

Material characterization: Infrared (IR) spectra were collected using a PerkinElmer Spectrum 100 spectrometer equipped with an attenuated total reflectance accessory. The

15

samples were first ground using an agate mortar and spectra were collected in the range of 650 – 4000 cm^{-1}. X-ray photoelectron spectroscopy (XPS) was performed on a Thermo Scientific K-Alpha[+] X-ray photoelectron spectrometer equipped with a MXR3 Al Kα monochromated X-ray source (hυ= 1486.6 eV). The samples were initially ground and mounted onto an XPS sample holder using a small piece of conductive carbon tape. The X-ray gun power was set to 72 W (6 mA and 12 kV). The high-resolution spectra were obtained using 20 eV pass energy and 0.1 eV step size. Thermo Avantage software was used to analyze the data. Powder X-ray diffraction (PXRD) patterns were recorded using a PANalytical X'Pert PRO diffractometer using Cu Kα radiation (λ = 1.54178 Å) with a step of 0.01 ° at a scanning speed of 10 s per step. An anode voltage of 40 kV and emission current of 20 mA were chosen as the operating conditions. Scanning electron microscope (SEM) images were taken using a Zeiss Auriga microscope with an accelerating voltage of 5 kV. The samples were placed on the carbon tape without grinding and coated with 15 nm of gold. N_2 adsorption isotherms were undertaken at 77 K, using a Micromeritics 3Flex instrument. The samples were initially degassed overnight at 120 °C at approximately 0.2 mbar pressure. Prior to the sorption isotherm measurement, the samples were further degassed in-situ for 4 h at 120 °C. The equivalent specific surface areas of the samples were determined using the Brunauer-Emmett-Teller (BET) method.[53] The total pore volume was evaluated from the volume of N_2 adsorbed at a relative pressure (P/P$_0$) of 0.97. The micropore volume was determined using the Dubinin-Radushkevich model.[54] The pore size distribution was derived from the built-in software from Micromeritics, using DFT model for carbon slit shape pores. Rate of adsorption data was logged by intercepting the raw 3Flex data output using PuTTy. Mercury porosimetry was employed up to a final pressure of 2300 bar using an AutoPore IV 9500 instrument from Micromeritics to measure the bulk density. Prior to the analysis, the samples were activated overnight at 120 °C under vacuum.

Moisture stability test: A vial with 20 mL of DI water was placed in a 1 L sealed container until the relative humidity reached >99 %, which was measured by a hygrometer. $_{mp}$BN was

kept in the container for different durations before it was collected and dried at 120 °C under vacuum.

Mechanical stability test: The hardness of $_{mp}$BN was measured using a Struers Duramin -1/-2 Micro-Vickers hardness tester, following the Vickers method. A load of 0.025 kgf (1 kgf = 9.8 N) was applied with a dwell time of 12 s. For each sample, at least 10 indentations were performed at different points. The samples were polished on 2000 grit sandpaper with a Struers TegraPol-31 polisher before the measurement.

Methane adsorption isotherms: High-pressure CH_4 adsorption isotherms were carried out at 298 K in the pressure range of 0-70 bar using the equipment and method reported before.[55] In brief, CH_4 uptake was measured gravimetrically using a Rubotherm Magnetic Suspension Balance (MSB) with an equilibration time of at least 90 min for each pressure point. The samples were initially degassed in a vacuum oven overnight at 393 K and approximately 0.2 mbar pressure. Prior to the sorption isotherm measurement, the samples were further degassed in-situ for 12 h at 393 K and a Helium gravimetry experiment was carried out at 298 K to estimate the adsorbent skeletal density.

Supporting Information
Supporting Information is available below.

Conflict of Interest
The authors declare no conflict of interest.

References

[1]   B. M. Weckhuysen, J. Yu, *Chem. Soc. Rev.* **2015**, *44*, 7022.

[2]   M. R. Benzigar, S. N. Talapaneni, S. Joseph, K. Ramadass, G. Singh, J. Scaranto, U. Ravon, K. Al-Bahily, A. Vinu, *Chem. Soc. Rev.* **2018**, *47*, 2680.

[3]   H. C. J. Zhou, S. Kitagawa, *Chem. Soc. Rev.* **2014**, *43*, 5415.

[4]   M. I. Nandasiri, S. R. Jambovane, B. P. McGrail, H. T. Schaef, S. K. Nune, *Coord. Chem. Rev.* **2016**, *311*, 38.

[5]   A. Feinle, M. S. Elsaesser, N. Hüsing, *Chem. Soc. Rev.* **2016**, *45*, 3377.

[6]   Y. Peng, V. Krungleviciute, I. Eryazici, J. T. Hupp, O. K. Farha, T. Yildirim, *J. Am. Chem. Soc.* **2013**, *135*, 11887.

[7]   J. Hou, A. F. Sapnik, T. D. Bennett, *Chem. Sci.* **2020**, *11*, 310.

[8]   T. Tian, J. Velazquez-Garcia, T. D. Bennett, D. Fairen-Jimenez, *J. Mater. Chem. A* **2015**, *3*, 2999.

[9]   T. Tian, Z. Zeng, D. Vulpe, M. E. Casco, G. Divitini, P. A. Midgley, J. Silvestre-Albero, J. C. Tan, P. Z. Moghadam, D. Fairen-Jimenez, *Nat. Mater.* **2018**, *17*, 174.

[10]   E. C. Hammel, O. L. R. Ighodaro, O. I. Okoli, *Ceram. Int.* **2014**, *40*, 15351.

[11]   P. Dibandjo, F. Chassagneux, L. Bois, C. Sigala, P. Miele, *J. Mater. Chem.* **2005**, *15*, 1917.

[12]   S. Schlienger, J. Alauzun, F. Michaux, L. Vidal, J. Parmentier, C. Gervais, F.

Babonneau, S. Bernard, P. Miele, J. B. Parra, *Chem. Mater.* **2012**, *24*, 88.

[13]   Q. Weng, X. Wang, Y. Bando, D. Golberg, *Adv. Energy Mater.* **2014**, *4*, 1.

[14]   J. Li, X. Xiao, X. Xu, J. Lin, Y. Huang, Y. Xue, P. Jin, J. Zou, C. Tang, *Sci. Rep.* **2013**, *3*, 1.

[15]   S. Marchesini, A. Regoutz, D. Payne, C. Petit, *Microporous Mesoporous Mater.* **2017**, *243*, 154.

[16]   J. Dai, X. Wu, J. Yang, X. C. Zeng, *J. Phys. Chem. Lett.* **2014**, *5*, 393.

[17]   Q. Weng, X. Wang, C. Zhi, Y. Bando, D. Golberg, *ACS Nano* **2013**, *7*, 1558.

[18]   J. Ye, X. Zhu, B. Cheng, J. Yu, C. Jiang, *Environ. Sci. Technol. Lett.* **2017**, *4*, 20.

[19]   S. Marchesini, X. Wang, C. Petit, *Front. Chem.* **2019**, *7*.

[20]   S. Marchesini, C. M. McGilvery, J. Bailey, C. Petit, *ACS Nano* **2017**, *11*, 10003.

[21]   W. Lei, D. Portehault, D. Liu, S. Qin, Y. Chen, *Nat. Commun.* **2013**, *4*, 1777.

[22]   F. Liu, J. Yu, X. Ji, M. Qian, *ACS Appl. Mater. Interfaces* **2015**, *7*, 1824.

[23]   R. Shankar, M. Sachs, L. Francàs, D. Lubert-Perquel, G. Kerherve, A. Regoutz, C. Petit, *J. Mater. Chem. A* **2019**, *7*, 23931.

[24]   Q. Weng, B. Wang, X. Wang, N. Hanagata, X. Li, D. Liu, X. Wang, X. Jiang, Y. Bando, D. Golberg, *ACS Nano* **2014**, *8*, 6123.

[25]   J. Lin, X. Yuan, G. Li, Y. Huang, W. Wang, X. He, C. Yu, Y. Fang, Z. Liu, C. Tang, *ACS Appl. Mater. Interfaces* **2017**, *9*, 44732.

[26]   G. Li, M. Zhu, W. Gong, R. Du, A. Eychmüller, T. Li, W. Lv, X. Zhang, *Adv. Funct. Mater.* **2019**, *29*, 1.

[27] M. Rousseas, A. P. Goldstein, W. Mickelson, M. A. Worsley, L. Woo, A. Zettl, *ACS Nano* **2013**, *7*, 8540.

[28] Y. Song, B. Li, S. Yang, G. Ding, C. Zhang, X. Xie, *Sci. Rep.* **2015**, *5*, 1.

[29] X. Xu, Q. Zhang, M. Hao, Y. Hu, Z. Lin, L. Peng, T. Wang, X. Ren, C. Wang, Z. Zhao, C. Wan, H. Fei, L. Wang, J. Zhu, H. Sun, W. Chen, T. Du, B. Deng, G. J. Cheng, I. Shakir, C. Dames, T. S. Fisher, X. Zhang, H. Li, Y. Huang, X. Duan, *Science (80-.).* **2019**, *363*, 723.

[30] Y. Xue, P. Dai, X. Jiang, X. Wang, C. Zhang, D. Tang, Q. Weng, X. Wang, A. Pakdel, C. Tang, Y. Bando, D. Golberg, *J. Mater. Chem. A* **2015**, *4*, 1469.

[31] S. Bernard, P. Miele, *New J. Chem.* **2014**, *38*, 1923.

[32] N. H. Ray, B. C. Lane, B. Shaw, US Patent 3931064, **1976**.

[33] R. Shankar, S. Marchesini, C. Petit, *J. Phys. Chem. C* **2019**, *123*, 4282.

[34] M. Thommes, K. Kaneko, A. V. Neimark, J. P. Olivier, F. Rodriguez-Reinoso, J. Rouquerol, K. S. W. Sing, *Pure Appl. Chem.* **2015**, *87*, 1051.

[35] H. Giesche, In *Handbook of Porous Solids*, Wiley-VCH Verlag GmbH, Weinheim, Germany, **2008**, pp. 309–351.

[36] J. G. Alauzun, S. Ungureanu, N. Brun, S. Bernard, P. Miele, R. Backov, C. Sanchez, *J. Mater. Chem.* **2011**, *21*, 14025.

[37] X. Zeng, L. Ye, S. Yu, R. Sun, J. Xu, C. P. Wong, *Chem. Mater.* **2015**, *27*, 5849.

[38] Y. Joo Jeong, M. F. Islam, *Nanoscale* **2015**, *7*, 12888.

[39] M. Wang, T. Zhang, D. Mao, Y. Yao, X. Zeng, L. Ren, Q. Cai, S. Mateti, L. H. Li, X.

Zeng, G. Du, R. Sun, Y. Chen, J. Bin Xu, C. P. Wong, *ACS Nano* **2019**, *13*, 7402.

[40]   W. Lei, V. N. Mochalin, D. Liu, S. Qin, Y. Gogotsi, Y. Chen, *Nat. Commun.* **2015**, *6*, 1.

[41]   C. N. Yeh, H. Huang, A. T. O. Lim, R. H. Jhang, C. H. Chen, J. Huang, *Nat. Commun.* **2019**, *10*.

[42]   J. H. Pikul, S. Özerinç, B. Liu, R. Zhang, P. V. Braun, V. S. Deshpande, W. P. King, *Sci. Rep.* **2019**, *9*, 1.

[43]   H. Kashani, Y. Ito, J. Han, P. Liu, M. Chen, *Sci. Adv.* **2019**, *5*, 1.

[44]   T. Woignier, J. Primera, A. Alaoui, F. Despetis, S. Calas-Etienne, A. Faivre, L. Duffours, C. Levelut, P. Etienne, *J. Sol-Gel Sci. Technol.* **2020**, *93*, 6.

[45]   S. Zhuang, E. S. Lee, L. Lei, B. B. Nunna, L. Kuang, W. Zhang, *Int. J. Energy Res.* **2016**, *40*, 2136.

[46]   A. Deryło-Marczewska, J. Goworek, S. Pikus, E. Kobylas, W. Zgrajka, *Langmuir* **2002**, *18*, 7538.

[47]   J. Jana, M. Ganguly, K. R. S. Chandrakumar, G. M. Rao, T. Pal, *Langmuir* **2017**, *33*, 573.

[48]   H. Fang, C. Yu, T. Ma, J. Qiu, *Chem. Commun.* **2014**, *50*, 3328.

[49]   S. Dyjak, W. Kiciński, A. Huczko, *J. Mater. Chem. A* **2015**, *3*, 9621.

[50]   T. S. Miller, A. B. Jorge, T. M. Suter, A. Sella, F. Corà, P. F. McMillan, *Phys. Chem. Chem. Phys.* **2017**, *19*, 15613.

[51]   Y. Gong, G. Shi, Z. Zhang, W. Zhou, J. Jung, W. Gao, L. Ma, Y. Yang, S. Yang, G.

You, R. Vajtai, Q. Xu, A. H. Macdonald, B. I. Yakobson, J. Lou, Z. Liu, P. M. Ajayan, *Nat. Commun.* **2014**, *5*.

[52]   C. Wu, B. Wang, N. Wu, C. Han, X. Zhang, S. Shen, Q. Tian, C. Qin, P. Li, Y. Wang, *Ceram. Int.* **2020**, *46*, 1083.

[53]   S. Brunauer, P. H. Emmett, E. Teller, *J. Am. Chem. Soc.* **1938**, *60*, 309.

[54]   S. G. Chen, R. T. Yang, *Langmuir* **1994**, *10*, 4244.

[55]   H. Ansari, L. Joss, J. Hwang, J. P. M. Trusler, G. Maitland, R. Pini, *Microporous Mesoporous Mater.* **2020**, *308*, 110537.

Supporting Information

Mechanically stable monolithic porous boron nitride with high volumetric adsorption capacity

Tian Tian, Jingwei Hou, Humera Ansari, Ying Xiong, Anouk L'Hermitte, David Danaci, Ronny Pini, and Camille Petit*

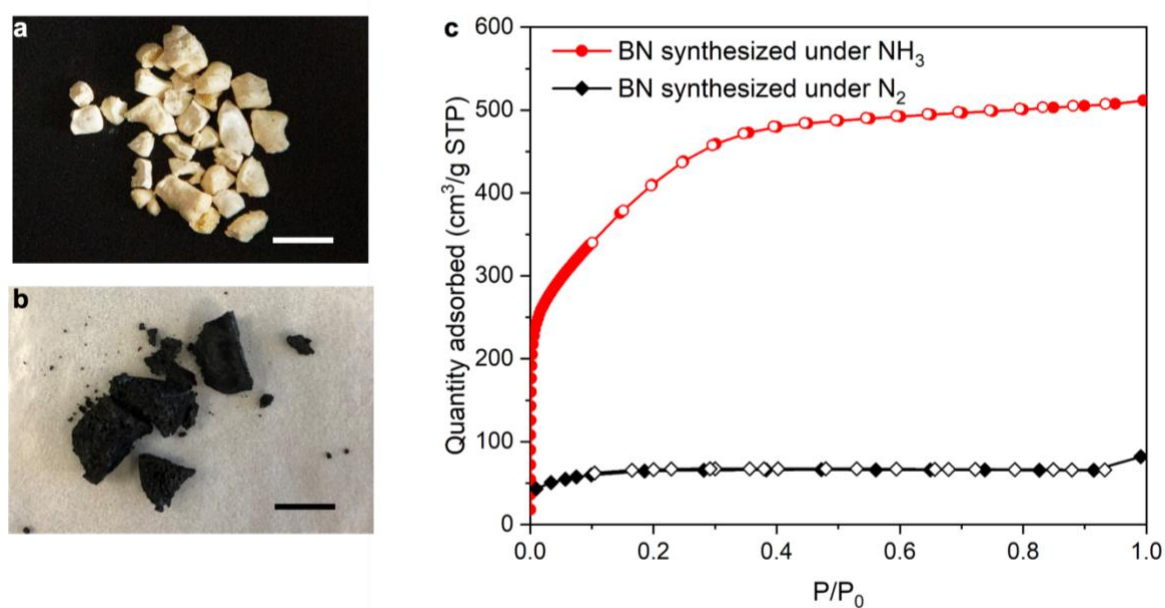## 1. Synthesis of monolithic porous ($_{mp}$BN)

1.1. Effects of dicyandiamide (DCD)
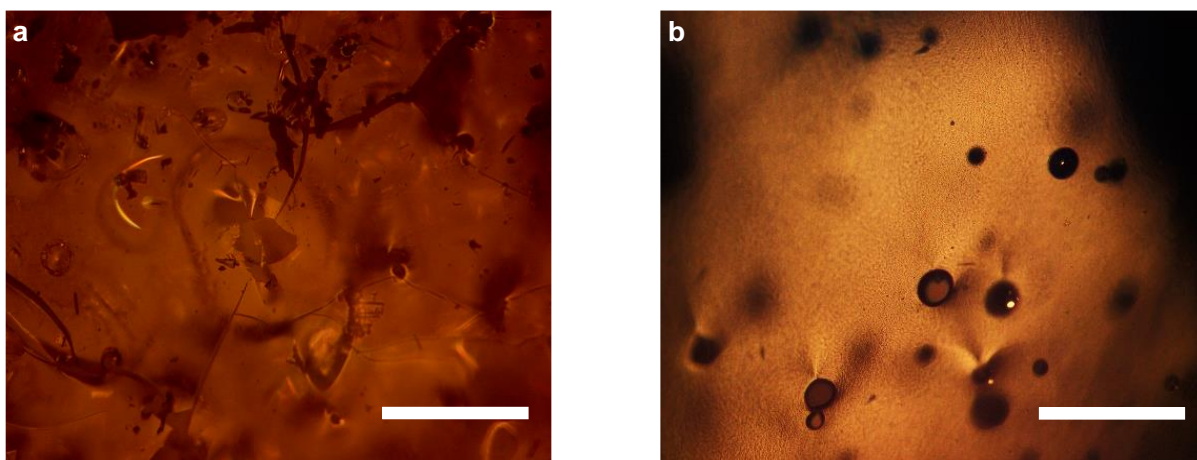
Figure S1. Microscope images of MF resin with (a) 0.5 g DCD and (b) 1.5 g DCD. Scale bar = 100 µm.

Figure S2. Optical image of MF resin with 1.5 g DCD before the transparent samples were collected.

1.2. Effects of reaction gas on $_{mp}$BN

Figure S3. Optical images of porous BN obtained under (a) NH$_3$ and (b) N$_2$. Scale bar = 1 cm. c) N$_2$ sorption isotherms at 77 K for BN synthesized under NH$_3$ (red circles) and N$_2$ (black diamonds).

2. Moisture stability of monolithic BN (mpBN) and powder BN

The hydrolytic instability of porous BN has been highlighted in previous studies and represents a major barrier to industrial applications.[1,2] Figures S4 and S5 show the influence of moisture (> 99% humidity) exposure time on the BET area of mpBN and powder BN. Both samples show virtually the same BET areas after the first hour. However, the porosity decreased significantly after 2 h of exposure for powder BN, showing a 54% loss in the surface area. For mpBN, the reduction was of 18%. More importantly, mpBN maintains more than 60% of its original surface area after 8 h exposure, whereas powder BN only retains 15%. A 25% more drop of the surface area is observed for mpBN after further 4 h exposure, at which point powder BN is virtually non-porous.

We analyzed structural changes in both samples upon exposure to moisture using XRD. In the case of powder BN (Figure S4b), the (002) peak related to hexagonal BN increases in intensity and shifts to higher angles after exposure to moisture. This observation agrees with previous studies and indicates a loss of the amorphous portion of BN upon decomposition in water, leaving the residual material with a higher crystallinity (i.e. lower porosity and surface area).[3] mpBN exhibits a different trend (Figure S4c). The sample does not show any increase in crystallinity before 12 h of exposure. This observation suggests a slower degradation compared to powder BN, consistent with the BET area trend (Figure S5a). We attribute the greater hydrolytic stability of mpBN compared to that of powder BN to its lower content of oxygen atom (3 at% *vs* 9 at%). Indeed, oxygen sites are susceptible to hydrolysis attack as observed in other studies.[2]

26
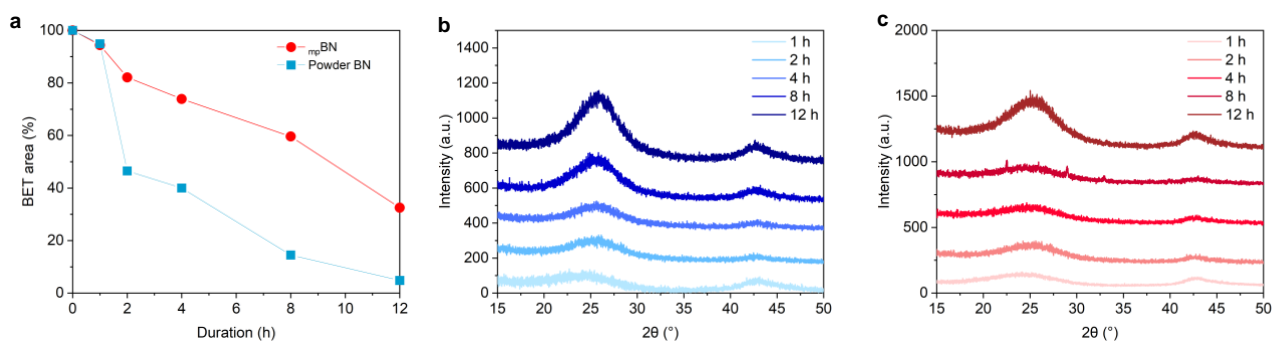
Figure S4. Structural features of monolithic porous BN (mpBN) and powder BN after moisture exposure. (a) BET surface area loss as derived from N_2 sorption at 77 K; (b) XRD patterns of powder BN; (c) XRD patterns of mpBN.
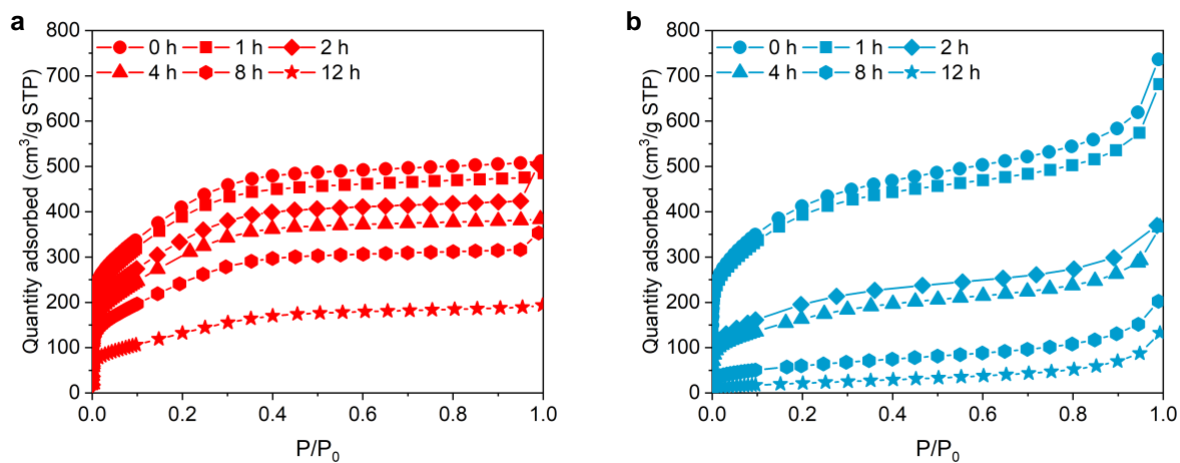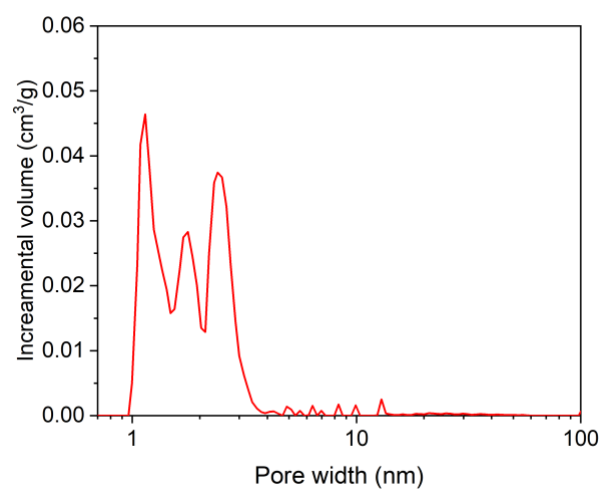
Figure S5. N₂ adsorption isotherms at 77 K after moisture exposure: (a) structured BN; (b) powder BN; 0 h, circle; 1 h, square; 2 h, diamond; 4 h, triangle; 8 h, hexagon; 12 h, star.

3. Gas adsorption: monolithic porous BN (mpBN) *vs* powder BN

3.1. N$_2$ adsorption isotherms at 77K.
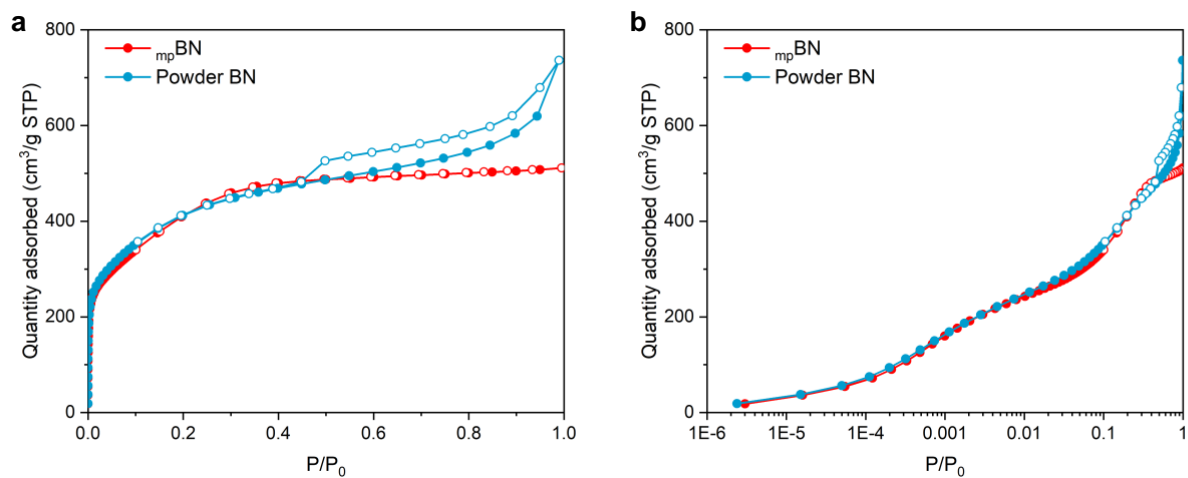
Figure S6. N$_2$ adsorption isotherms at 77 K for mpBN and powder BN in a) linear scale; b) semi-logarithmic scale.

Figure S7. Pore size distribution of $_{mp}$BN as derived from N_2 adsorption isotherms at 77 K.

3.2. Bulk density measurement via mercury porosimetry.

We measured the bulk density of both $_{mp}$BN and powder BN using mercury porosimetry, a well-established technique that has been used to measure the bulk density of other porous materials. Mercury is a non-wetting liquid that does not intrude into small pores at ambient pressure, facilitating the measurement of bulk volume, which includes both the material volume and the interstitial volume, and thus the bulk density.

   In a typical mercury intrusion porosimetry measurement, the sample is filled in a penetrometer, which has a known weight and volume. It should be noted that the sample is not mechanically compressed. After evacuation, the penetrometer is filled with mercury. The mercury will surround the sample at ambient pressure but not enter pores and voids smaller than ca. 6 µm. The weight of mercury is obtained by reweighing the penetrometer and by subtracting the known weights of the empty penetrometer and the sample. The volume of intruded mercury is then computed from the known mercury density (13.5394 g mL^{-1}) and the bulk volume of the sample is obtained as the difference between the empty penetrometer volume and the intruded mercury volume.

   As powder BN and $_{mp}$BN has the same composition and similar surface area, the materials volume of both samples can be exactly same. However, due to the more packed structure of $_{mp}$BN (i.e. less interparticle volume), the $_{mp}$BN shows much higher bulk density compared to powder BN.

3.3. Methane adsorption isotherms at 298 K.

The data of high-pressure methane uptake was obtained as excess gravimetric adsorption capacity (N_{exc}), and was converted into absolute gravimetric capacity (N_{abs}) using equation 1:

$$N_{abs} = N_{exc} + \rho_{gas}V_{micro} \qquad (1)$$

where ρ_{gas} is the density of the non-adsorbed gas and V_{micro} is the micropore volume of the adsorbent. The skeleton volumes (0.474 cm^3 g^{-1} for powder BN and 0.476 cm^3 g^{-1} for $_{mp}$BN) obtained by helium gravimetry were used to calculate the excess adsorbed capacity.[4]

Absolute volumetric adsorption capacity is converted from the absolute gravimetric uptake by multiplying by the *bulk density*. Bulk density is the ratio of the mass of an uncompressed solid sample and its volume, including the volume of the solid and the interparticle space.
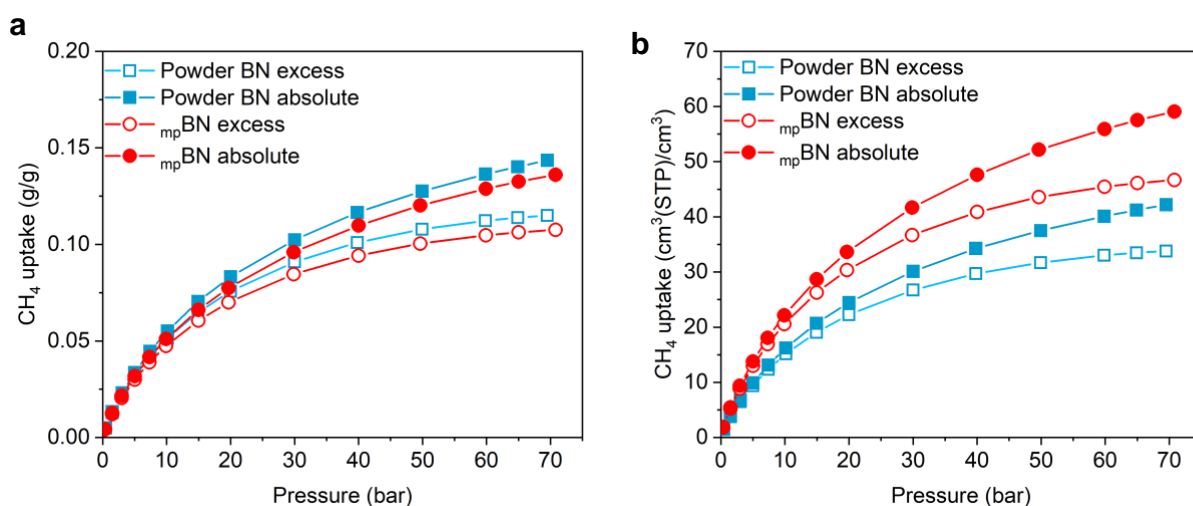
Figure S8. Comparison of absolute methane uptake at 298 K between powder BN (blue squares) and $_{mp}$BN (red circles): a) gravimetric uptake; b) volumetric uptake.

3.3. N₂ adsorption kinetics at 77 K
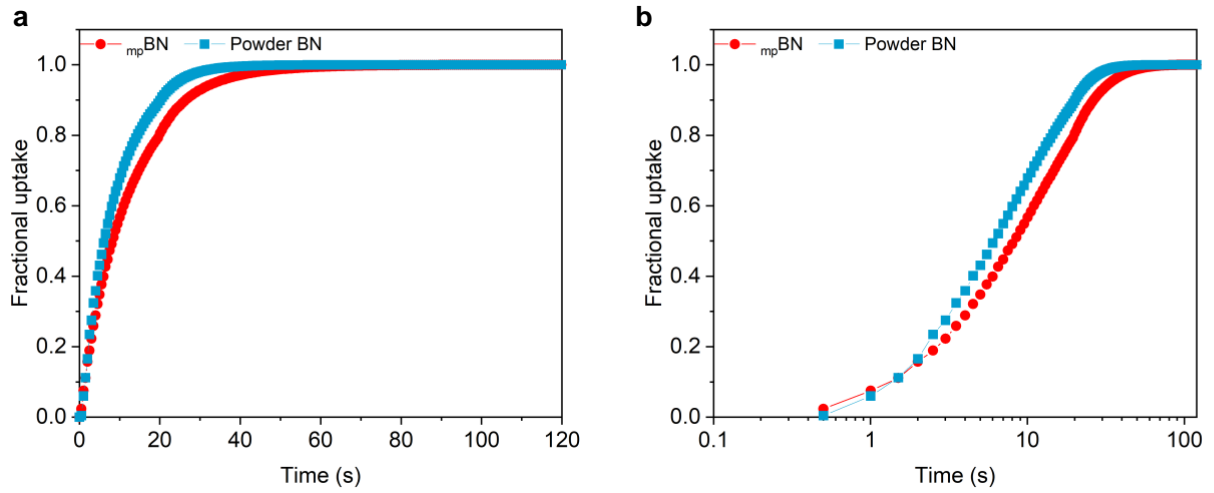
Figure S9. Comparison of adsorption kinetics of N_2 uptake at 77K and 2.2×10^{-6} bar between powder BN (blue) and mpBN (red circles): (a) linear scale, (b) semi-logarithmic scale.

Fractional uptake based on Equation 2 is used to study the adsorption kinetics:

$$Fractional\ uptake = \frac{m_t - m_o}{m_{eq} - m_0} \tag{2}$$

where m_t is the adsorption amount at time t, m_0 is the adsorption amount at t = 0, and m_{eq} is the adsorption amount at equilibrium.

## 4. Mechanical stability of monolithic porous BN ($_{mp}$BN)
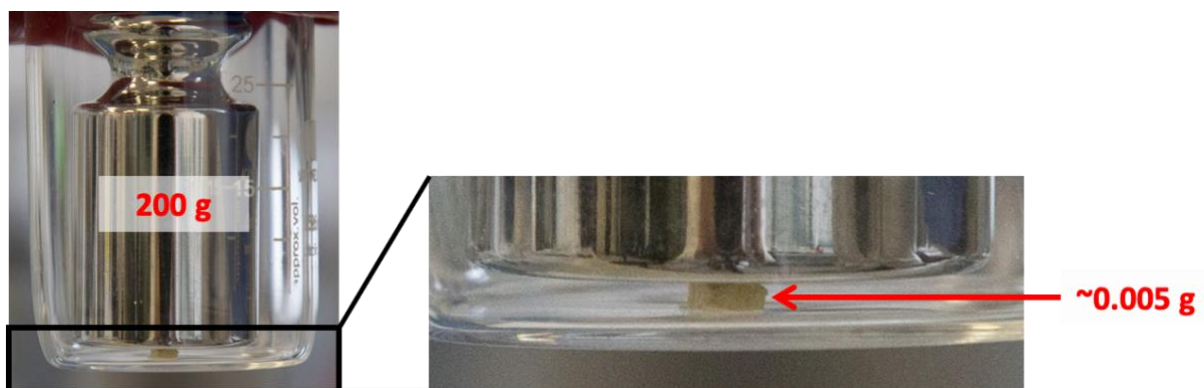
Figure S10. Optical image of structured porous BN under a 200 g calibration weight.

The mechanical stability is evaluated by Vickers microhardness test. To convert the Vickers hardness to SI unit (e.g. MPa), the value is multiplied by 9.807.[5]

5. Formation mechanism

FTIR was used to analyze the chemical composition of the intermediates. Sample collected at 200 °C shows NH$_2$ stretching band (3350 cm^{-1}), C-N stretching band (1560, 1450, 1320 cm^{-1}) and a triazine ring bending band (807 cm^{-1}).[6] All these bands indicate the successful synthesis of the MF resin. Because of the high mechanical strength of MF resin, which can be broken into small glassy pieces, together with the low content of B, the band attributed to B-containing bonds was not observed. Increasing the temperature to 300 °C leads to a new C-O stretching band at 1320 cm^{-1}. Both intermediates collected at 300 and 400 °C present an unknown band at around 880-890 cm^{-1}. This band is always present in melon-based materials, indicating the existence of melon-based polymer.[6] A new B-O stretching band (1390 cm^{-1}) is observed at 400 °C due to the increased percentage of B in the mixture.[7–10] A very broad band between 800-1700 cm^{-1} at 600 °C indicates the phase transition process at this temperature. Three main characteristic bands (~1360, 1100, 790 cm^{-1}) belonging to BN appear when the temperature increased to 800 °C clearly suggested the formation of BN. The IR features remained unchanged when the temperature increased to 1000 °C. The FTIR analysis supports the formation mechanism hypothesis concluded from XPS analysis.
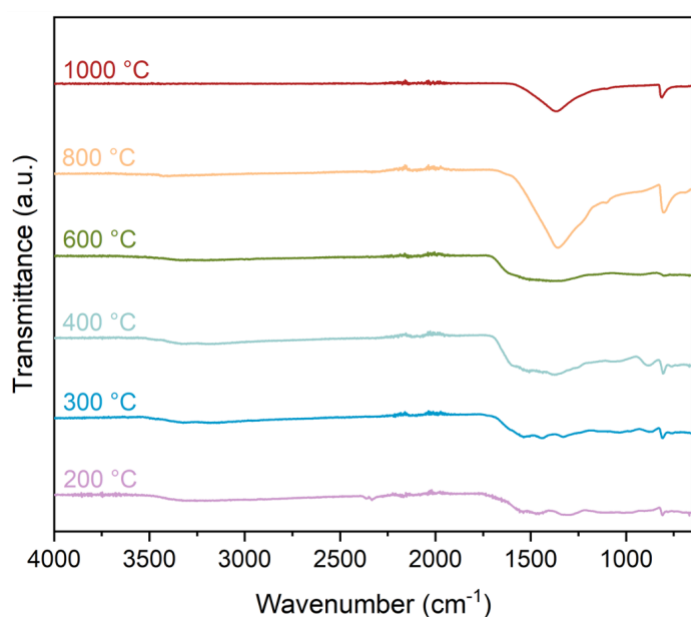
Figure S11. FTIR of intermediates obtained at different temperatures.

References

[1]   C. G. Cofer, J. Economy, *Carbon N. Y.* **1995**, *33*, 389.

[2]   R. Shankar, S. Marchesini, C. Petit, *J. Phys. Chem. C* **2019**, *123*, 4282.

[3]   W. Lei, V. N. Mochalin, D. Liu, S. Qin, Y. Gogotsi, Y. Chen, *Nat. Commun.* **2015**, *6*, 1.

[4]   H. Ansari, L. Joss, J. Hwang, J. P. M. Trusler, G. Maitland, R. Pini, *Microporous Mesoporous Mater.* **2020**, *308*, 110537.

[5]   M. M. Yovanovich, *Collect. Tech. Pap. - 44th AIAA Aerosp. Sci. Meet.* **2006**, *16*, 11702.

[6]   X. Wei, Y. Qiu, W. Duan, Z. Liu, *RSC Adv.* **2015**, *5*, 26675.

[7]   C. Wu, B. Wang, N. Wu, C. Han, X. Zhang, S. Shen, Q. Tian, C. Qin, P. Li, Y. Wang, *Ceram. Int.* **2020**, *46*, 1083.

[8]   X. Qiao, Z. Zhou, X. Liu, C. Zhao, Q. Guan, W. Li, *Catal. Sci. Technol.* **2019**, *9*, 3753.

[9]   J. Xu, Y. Li, S. Peng, G. Lu, S. Li, *Phys. Chem. Chem. Phys.* **2013**, *15*, 7657.

[10]   S. J. Makowski, P. Köstler, W. Schnick, *Chem. - A Eur. J.* **2012**, *18*, 3248.